

Magnetotransport in spin-orbit coupled noncentrosymmetric and Weyl metals

Gautham Varma K,¹ Azaz Ahmad,¹ Sumanta Tewari,² and G. Sharma¹

¹*School of Physical Sciences, Indian Institute of Technology Mandi, Mandi 175005, India.*

²*Department of Physics and Astronomy, Clemson University, Clemson, SC 29631, USA.*

Recently, chiral anomaly (CA) has been proposed to occur in spin-orbit coupled non-centrosymmetric metals (SOC-NCMs), motivating CA to be a Fermi surface property rather than a Weyl node property. Although the nature of the anomaly is similar in both SOC-NCMs and Weyl systems, here we point out significant fundamental differences between the two. We show that the different nature of the orbital magnetic moment (OMM) in the two systems leads to nontrivial consequences— particularly the sign of the longitudinal magnetoconductance always remains positive in a SOC non-centrosymmetric metal, unlike a Weyl metal that displays either sign. Furthermore, we investigate the planar Hall effect and the geometrical contribution to the Hall effect in the two systems and point out significant differences in the two systems. We conduct our analysis for magnetic and non-magnetic impurities, making our study important in light of current and upcoming experiments in both SOC-NCMs and Weyl metals.

I. INTRODUCTION

Chiral anomaly roots its origin in high-energy physics [1, 2]. It refers to the non-conservation of left and right-handed Weyl fermions separately in the presence of external gauge fields. Over the past decade, its unexpected appearance in solid-state systems has caused great excitement in the condensed matter community [3–31]. Specifically, Weyl fermions, discovered as electronic excitations in specific systems (termed as Weyl semimetals (WSMs)), can manifest the anomaly that can be detected via relatively simple transport [10–16] or optical [32–38] measurements. The key requirement is that the elementary excitations should be chiral and relativistic in odd spatial dimensions [39].

The realization of the anomaly has recently been extended to certain other systems distinct from Weyl semimetals [40–49]. Specifically, it has been suggested that the anomaly can be realized in spin-orbit-coupled (SOC) non-centrosymmetric metals (NCMs) that host nonrelativistic fermions with only one relevant band touching point [48]. The effect of the anomaly on charge and thermal transport properties of SOC-NCMs has recently been studied, and it has been suggested that the anomaly results in positive longitudinal magnetoconductance (LMC) [48, 49], akin to Weyl semimetals. The sign of LMC has been a subject of much debate and exploration in WSMs. It is expected to crucially depend on the nature of impurities, the strength of the magnetic field, and the strength of the intervalley scattering. Under strong magnetic fields, due to Landau quantization, the LMC sign depends on the nature of scattering impurities [30, 50–55].

Recently, we pointed out that the sign of LMC is, in fact, more nuanced [56]. LMC in Weyl systems can typically be expressed as $\sigma_{zz} = \sigma_0 + \sigma_{zz}^{(2)}(B - B_0)^2$. ‘Strong-sign-reversal’ is characterized by the reversal of orientation of the magnetoconductance parabola with respect to the magnetic field, while in ‘weak-sign-reversal,’ the magnetoconductivity depends on the direction of the mag-

netic field and is not correlated with the orientation of the LMC parabola. Fig. 1 (c) shows a schematic description of strong and weak-sign-reversal of LMC. Specifically, in the case of weak-sign-reversal, LMC is linear near zero magnetic field, while the vertex of the parabola (B_0) is shifted from the origin, but the quadratic coefficient of LMC ($\sigma_{zz}^{(2)}$) remains positive. In the case of strong-sign-reversal, importantly, the quadratic coefficient $\sigma_{zz}^{(2)}$ becomes negative. When Landau quantization can be ignored under weak magnetic fields, quasiclassical Boltzmann analysis suggests that sufficiently strong intervalley scattering can reverse the sign of LMC from positive to negative (strong-sign-reversal) [19, 20, 57]. Whether or not the longitudinal magnetoconductance in SOC-NCMs shows similar characteristics also remains an important and pertinent question in the field. Furthermore, the focus of all the previous works has been particularly on point-like scalar non-magnetic impurities. The fate of LMC in both spin-orbit-coupled and Weyl metals in the presence of (pseudo)magnetic impurities remains to be determined.

In SOC-NCMs, we focus on the vicinity of one nodal point surrounded by two Fermi surfaces as depicted in Fig. 2 (b). This is in contrast to the two separate nodal points and Fermi surfaces we are concerned with in WSMs (Fig. 2 (a)). The role of intranode scattering in WSMs is replaced by intraband scattering in SOC-NCMs. This scattering preserves the chirality of the scattered quasiparticles. Internode scattering in WSMs is equivalent to interband scattering in SOC-NCMs, reversing the quasiparticle chirality. Internode scattering in WSMs requires the transfer of large momentum of the order of separation between the Weyl nodes, which is usually weaker than intranode scattering requiring a small momentum transfer. In contrast, in SOC-NCMs, the momentum transfer with interband scattering is not necessarily small, as both the Fermi surfaces surround a single nodal point. Thus, interband scattering is expected to be at least as significant in SOC-NCMs as it is in WSMs, and its exploration remains an open question.

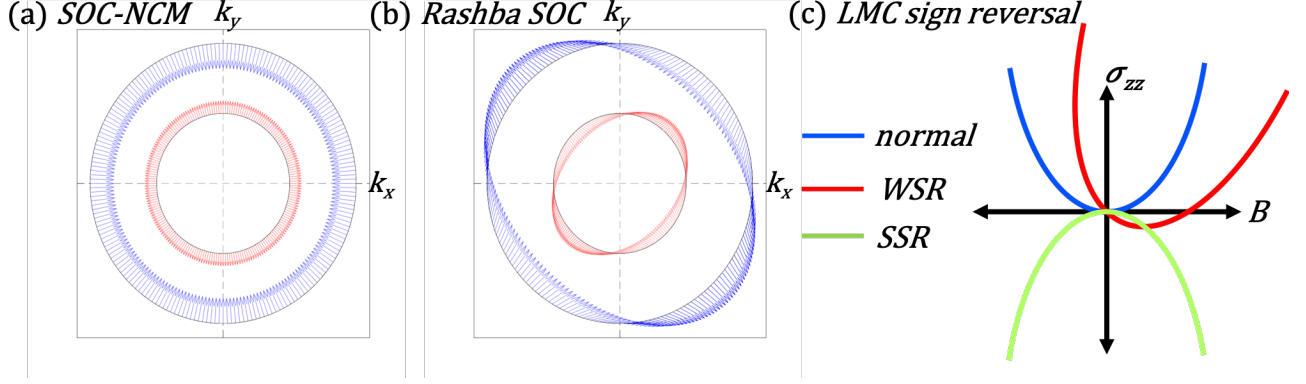


Figure 1. Spin texture of (a) SOC-NCM in the $k_z = 0$ plane, and (b) a Rashba coupled system. The arrows point in the direction of the spin expectation value \mathbf{S}^λ . Blue and red arrows are for the outer and inner Fermi surfaces, respectively. (c) Schematic figure representing weak-sign-reversal (WSR) and strong-sign-reversal (SSR) compared to normal LMC in Weyl systems.

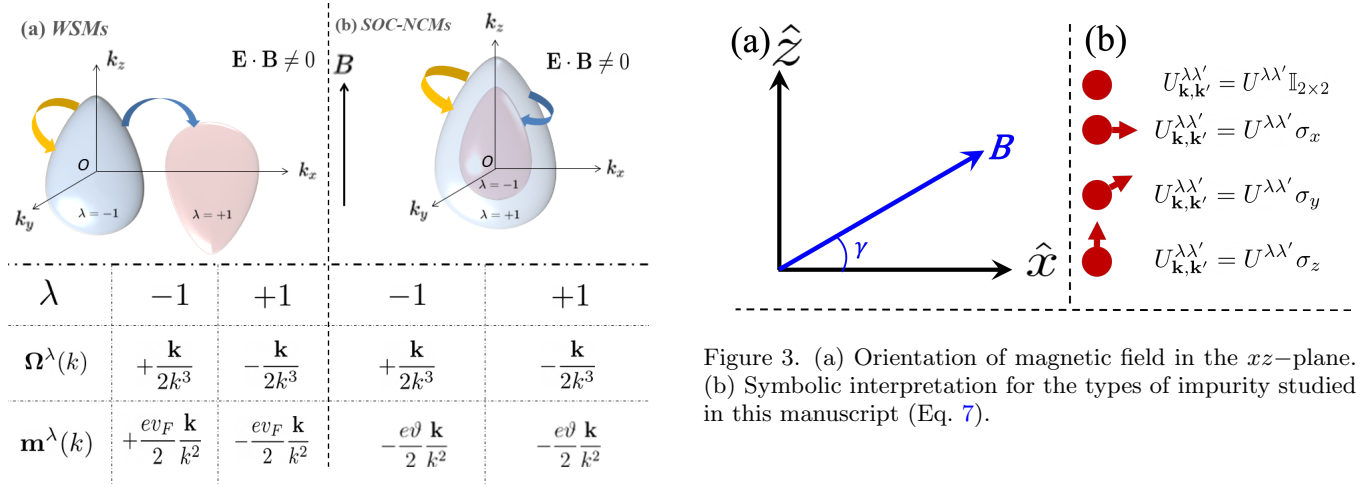


Figure 2. Quasiparticle scattering in WSMs (a) and SOC-NCMs (b). Unlike WSMs, quasiparticle scattering in SOC-NCMs occurs between the surfaces (FSs) associated with a single nodal point. The two Fermi FSs in SOC-NCMs have opposite Berry curvature ($\Omega^\lambda(\mathbf{k})$), but crucially, unlike WSMs, have the same orbital magnetic moment ($\mathbf{m}^\lambda(\mathbf{k})$). Blue and yellow arrows represent the internode (interband for SOC-NCMs) and intranode (intra-band for SOC-NCMs) scattering, respectively, in WSMs. Here, λ is the band/node index. The oval shape of the Fermi surfaces is due to the coupling of the orbital magnetic moment in an external magnetic field.

In this work, we probe the role of interband scattering in SOC-WSMs and show that in the quasiclassical low-field regime, unlike WSMs, the sign of LMC is *not* sensitive to the relative strength of the interband scattering. Longitudinal magnetoconductance in SOC-NCMs is found to be always positive, irrespective of the strength of the interband scattering. We trace the reason to the orbital magnetic moment (OMM) in SOC-NCMs that is of equal magnitude and sign at both the bands, as compared to the case of WSMs where OMM has equal mag-

Figure 3. (a) Orientation of magnetic field in the xz -plane. (b) Symbolic interpretation for the types of impurity studied in this manuscript (Eq. 7).

nitudes but opposite signs at the two nodes (see Fig. 2). We examine how the subtle difference in OMM can lead to drastic differences in other transport properties, such as the planar Hall conductivity, and also give rise to a finite geometrical contribution to the Hall conductivity in SOC-NCMs. Furthermore, we also analyze all the properties of both WSMs and SOC-NCMs in the presence of both point-like scalar and magnetic impurities, which has remained an open problem so far.

II. MODEL AND FORMALISM

We begin with the following extended model of a spin-orbit coupled non-centrosymmetric metal that can be expressed near the high-symmetry point as

$$H_{\text{soc}}(\mathbf{k}) = \frac{\hbar^2 k^2}{2m} \sigma_0 + \hbar \vartheta \mathbf{k} \cdot \boldsymbol{\sigma} + \hbar \vartheta (k_x t_x + k_z t_z) \sigma_0 \quad (1)$$

Here, m is the effective electron mass. The second term represents the spin-orbit coupling term, and $\boldsymbol{\sigma}$ denotes the vector of Pauli matrices in the spin space. The third

term in the Hamiltonian tilts the dispersion along a particular direction, and the dimensionless parameters t_x and t_z represent the tilting along x - and z -direction, respectively. Similar to the case of WSMs, the tilt term may arise naturally in the bandstructure in SOC-NCMs or may model the effect of strain in the material.

It is instructive to also compare the above Hamiltonian to a Rashba coupled system given by

$$H_{\text{Rashba}}(\mathbf{k}) = \frac{\hbar^2 k^2}{2m} \sigma_0 + \alpha_R (k_x \sigma_y - k_y \sigma_x), \quad (2)$$

where α_R is the Rashba coefficient. The spin-texture for both H_{soc} and H_{Rashba} can be evaluated as $\mathbf{S}^\lambda = \langle u^\lambda(\mathbf{k}) | \boldsymbol{\sigma} | u^\lambda(\mathbf{k}) \rangle$, where $|u^\lambda(\mathbf{k})\rangle$ is the spinor wavefunction and λ is the band-index. The spin-texture for both the above Hamiltonians (Eq. 1 and Eq. 2) is given in Fig. 1. The spin rotates as we traverse along the Fermi surface. Importantly, the spins in the two Fermi surfaces point in the opposite direction to each other, indicating their opposite chirality.

To compare our results with WSM, we use the following prototype model of a two-node time-reversal symmetry broken WSM.

$$H_{\text{wsM}} = \left(\sum_{\chi=\pm 1} \hbar v_F \chi \mathbf{k} \cdot \boldsymbol{\sigma} \right) + \hbar v_F (k_x t_x + k_z t_z) \sigma_0. \quad (3)$$

Here, χ is the chirality and v_F is the Fermi velocity. The Hamiltonian in Eq.1 has the following energy dispersion

$$\epsilon^\lambda(\mathbf{k}) = \frac{\hbar^2 k^2}{2m} + \lambda \hbar v k + \hbar v (k_x t_x + k_z t_z) \quad (4)$$

Here, $\lambda = \mp 1$ is the band index. The corresponding eigenvectors are: $|u^\lambda\rangle^T = [\lambda e^{-i\phi} \cos(\theta/2), \sin(\theta/2)]$. We assume that the Fermi energy ϵ_F lies above the nodal point $\mathbf{k} = 0$, and thus we have two Fermi surfaces corresponding to the two energy bands as shown in Fig. 2 (b). The Berry curvature ($\boldsymbol{\Omega}_\mathbf{k}^\lambda$) for both these surfaces has equal magnitudes and opposite signs, just like the Fermi surfaces in the vicinity of two nodal points in WSMs. Interestingly, the orbital magnetic moment ($\mathbf{m}_\mathbf{k}^\lambda$) carries the same sign and magnitude, distinct from WSMs where the signs are reversed. In the presence of an external magnetic field (\mathbf{B}), the orbital magnetic moment couples to the dispersion as $-\mathbf{m}_\mathbf{k}^\lambda \cdot \mathbf{B}$ leading to the oval-shaped Fermi surfaces as shown in Fig. 2 (b). In WSMs, the coupling is opposite, and thus, the shapes of the surfaces are reversed.

We study charge transport in the presence of perturbative electric and magnetic fields using the quasiclassical Boltzmann formalism. This is valid in the limits of weak magnetic fields, $B \ll B_c$, where $eB_c \hbar / 2m \epsilon_F = 1$. The non-equilibrium distribution function $f_\mathbf{k}^\lambda$ obeys the following steady-state equation:

$$\dot{\mathbf{r}}_\mathbf{k}^\lambda \cdot \nabla_\mathbf{r} f_\mathbf{k}^\lambda + \dot{\mathbf{k}}^\lambda \cdot \nabla_\mathbf{k} f_\mathbf{k}^\lambda = I_{\text{coll}}[f_\mathbf{k}^\lambda]. \quad (5)$$

Here, $f_\mathbf{k}^\lambda = f_0 + g_\mathbf{k}^\lambda$, with f_0 being the Fermi-Dirac distribution and $g_\mathbf{k}^\lambda$ is the deviation due to the presence of the external fields. We restrict ourselves to the first order in the electric field, i.e., $g_\mathbf{k}^\lambda = -e \left(\frac{\partial f_0}{\partial \mu} \right)_{\epsilon_F} \mathbf{E} \cdot \boldsymbol{\Lambda}_\mathbf{k}^\lambda$. The collision integral (I_{coll}) in Eq. 5 is chosen in such a way that it can incorporate both interband and intraband scattering, given by

$$I_{\text{coll}}[f_\mathbf{k}^\lambda] = \sum_{\lambda'} \sum_{\mathbf{k}'} \mathbf{W}_{\mathbf{k}\mathbf{k}'}^{\lambda\lambda'} (f_{\mathbf{k}'}^{\lambda'} - f_\mathbf{k}^\lambda), \quad (6)$$

where, the scattering rate $\mathbf{W}_{\mathbf{k}\mathbf{k}'}^{\lambda\lambda'}$ calculated using the Fermi's golden rule,

$$\mathbf{W}_{\mathbf{k}\mathbf{k}'}^{\lambda\lambda'} = \frac{2\pi n}{\mathcal{V}} |\langle u^{\lambda'}(\mathbf{k}') | U_{\mathbf{k}\mathbf{k}'}^{\lambda\lambda'} | u^\lambda(\mathbf{k}) \rangle|^2 \delta(\epsilon_{\mathbf{k}'}^{\lambda'} - \epsilon_F) \quad (7)$$

Here, ‘ n ’ is the impurity concentration, ‘ \mathcal{V} ’ is the system volume, $|u^\lambda(\mathbf{k})\rangle$ is the spinor wavefunction, $U_{\mathbf{k}\mathbf{k}'}^{\lambda\lambda'}$ is the scattering potential profile, and ϵ_F is the Fermi energy. Here we choose $U_{\mathbf{k}\mathbf{k}'}^{\lambda\lambda'}$ in such a manner that it can include both magnetic and non-magnetic point-like scattering centers. In general $U_{\mathbf{k}\mathbf{k}'}^{\lambda\lambda'} = U^{\lambda\lambda'} \sigma_i$ with $i = 0, 1, 2, 3$, where $U^{\lambda\lambda'}$ distinguishes the interband ($\lambda \neq \lambda'$) and intraband ($\lambda = \lambda'$) scattering. Here, we work in the geometry represented in Fig. 3 (a), i.e., we fix the direction of the electric field along the z -direction and rotate the magnetic field in the xz -plane that makes an angle γ with respect to the x -axis. Further calculation details for the solution of the distribution function $f_\mathbf{k}^\lambda$ are presented in the Appendix. Finally, the current is evaluated as $\mathbf{j} = -e \sum_{\lambda} \sum_{\mathbf{k}} \dot{\mathbf{r}}_\mathbf{k}^\lambda f_\mathbf{k}^\lambda$, and the conductance tensor $\hat{\sigma}$ is given by $\hat{j}_\alpha = \sigma_{\alpha\beta} E_\beta$. Unless otherwise specified, we choose the following values for our calculations: $m = 10^{-32} \text{kg}$, $v = 5 \times 10^5 \text{ms}^{-1}$, $v_F = 10^6 \text{ms}^{-1}$, $\epsilon_F = 50 \text{meV}$.

III. RESULTS

A. Longitudinal Magnetoconductance

We first discuss longitudinal magnetoconductance for SOC-NCM and compare it with a standard WSM. We examine the behavior of each impurity type (magnetic and non-magnetic) individually. In Fig. 4 (b) we plot the LMC in SOC-NCM as a function of the magnetic field for different values of the relative interband scattering strengths α (the ratio of interband scattering strength to intraband scattering strength), for non-magnetic σ_0 -impurities as well as σ_z -magnetic impurities. The LMC is always positive for any value of α . This is in striking contrast to WSMs where LMC changes sign (strong sign-reversal [56]) when $\alpha > \alpha_c$ (Fig. 4 (a)).

In WSMs, the sign of the OMM is different at Fermi surfaces at both nodes. This breaks the symmetry between them, thus also breaking the symmetry between

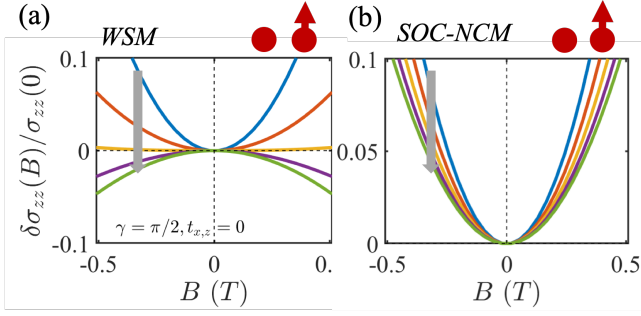


Figure 4. LMC in Weyl semimetals and SOC-NCMs as a function of the magnetic field for different values of the relative interband (internode for WSMs) scattering strengths α . As we move in the direction of the arrow from the blue to the green curve, α is increased from 0.35 to 1.25. We obtain the same behavior for a non-magnetic impurity profile i.e., $U_{\mathbf{k},\mathbf{k}'}^{\lambda\lambda'} = U^{\lambda\lambda'}\sigma_0$, as well as magnetic impurity i.e., $U_{\mathbf{k},\mathbf{k}'}^{\lambda\lambda'} = U^{\lambda\lambda'}\sigma_z$. (a) For WSM there is strong-sign-reversal above $\alpha > \alpha_c$, (b) For SOC-NCM, there is no sign-reversal for any interband scattering strength.

their chiral partners. This has been attributed to result in a strong-sign-reversal of LMC [19, 20, 56]. On the other hand, OMM shifts the energy dispersion in SOC-NCMs in both the Fermi surfaces by the same amount as shown in Fig. 2 (b). The symmetry between the chiral partners between both the Fermi surfaces thus remains intact and therefore no sign-reversal is observed. Since the magnetic- σ_z impurity doesn't flip the chirality of the quasiparticles in both SOC-NCMs and WSMs, we observe the same effect on LMC as a nonmagnetic impurity (σ_0). The σ_x and σ_y impurities, on the other hand, flip the chirality of the quasiparticles. We obtain quadratic and positive LMC for both WSMs and SOC-NCMs for σ_x and σ_y impurities (not plotted explicitly).

Next, we examine LMC as a function of the parameter t_z and α for σ_0 and σ_z impurities in Fig. 5. We obtain strikingly different behavior for WSMs and SOC-NCMs. For WSMs, the zero-LMC contour $\alpha_c(t_z)$, which separates positive and negative LMC, is now a function of t_z (Fig. 5 (a)). This change of sign corresponds to strong-sign-reversal. For SOC-NCMs, the zero-LMC contour appears for nonzero values of t_z and this change of sign is associated with weak-sign-reversal (Fig. 5 (b)). Specifically, the t_z -term tilts the parabola along a particular direction but does not flip its orientation.

In Fig. 5 (c) and Fig. 5 (d) we examine the behavior of LMC as a function of α and t_z for σ_x and σ_y -magnetic impurities. In WSMs, we observe weak-sign-reversal for large values of the tilt parameter t_z , and no sign-reversal for smaller values of t_z . Furthermore, increasing internode scattering restores positive LMC. This is in sharp contrast to the effect of σ_0 and σ_z impurities in WSMs, where we observe strong-sign-reversal and decreasing internode scattering restoring positive LMC. In SOC-NCMs, for σ_x and σ_y impurities, the effect of weak-

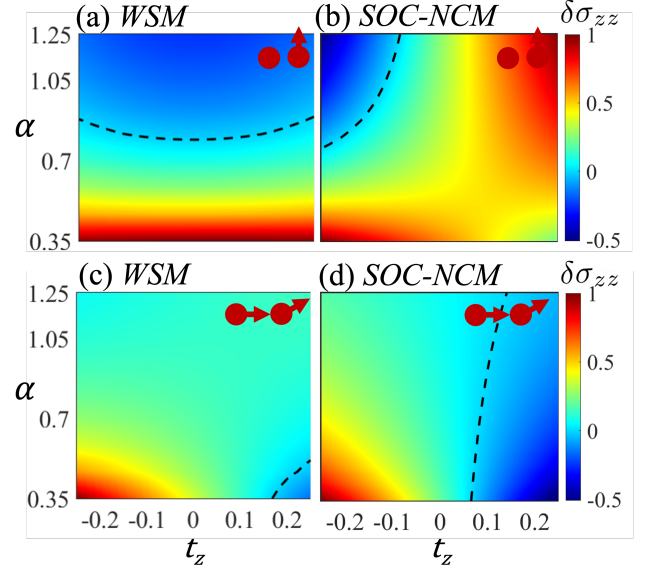


Figure 5. LMC in Weyl semimetals and SOC-NCMs as a function of the relative interband (internode for WSMs) scattering strengths α and the parameter t_z . The dashed black line shows the contour separating positive and negative LMC regions.

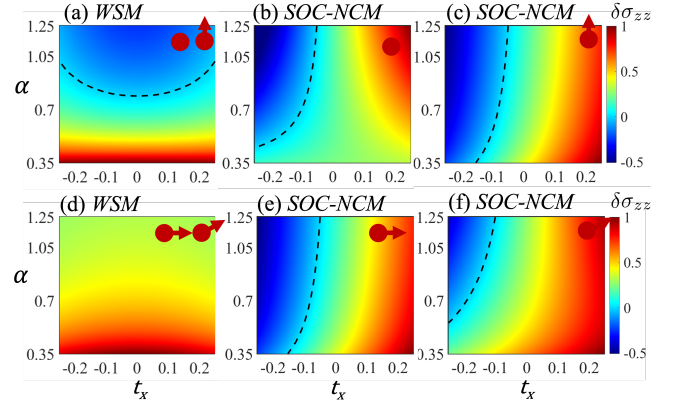


Figure 6. LMC in WSMs and SOC-NCMs in the presence of t_x parameter. The dashed black line shows the contour separating positive and negative LMC regions.

sign-reversal is more pronounced as shown in Fig. 5 (d). Again, larger interband scattering restores positive LMC. This feature is understood as follows. The σ_x (or σ_y) impurities flip the chirality of the fermions; further imposing interband scattering back-flips the reversed chirality, and thus interband σ_x scattering behaves like intraband scattering.

In Fig. 6 we compare the behavior of LMC of WSM with that of SOC-NCM in the presence of the tilt parameter t_x . In WSM, just like the case when $t_z \neq 0$, we find that the behavior in the presence of non-magnetic and σ_z -impurities is similar; we observe strong-sign-reversal.

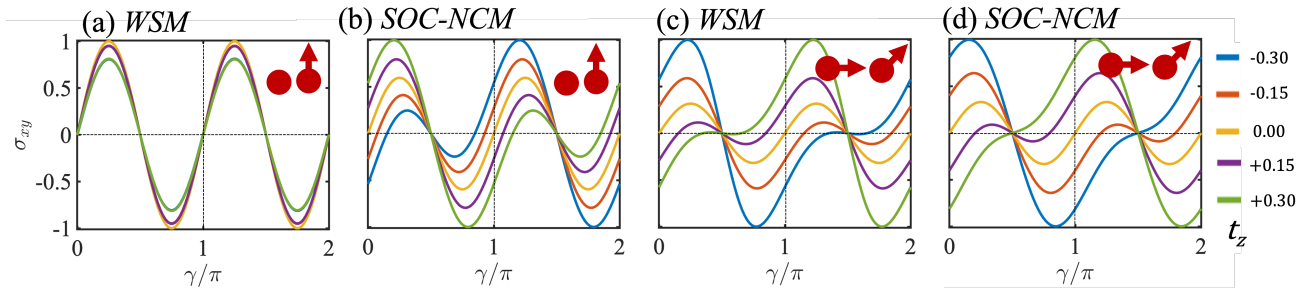


Figure 7. Planar Hall conductivity for WSM and SOC-NCM for different impurity types in the presence of parameter t_z . Plots are appropriately normalized.

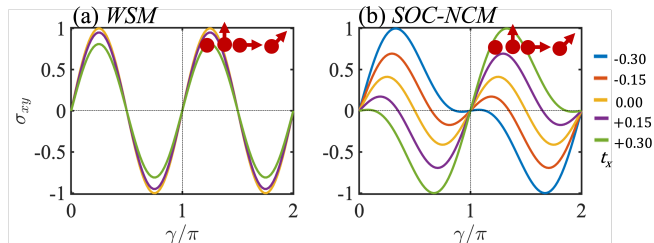


Figure 8. Planar Hall conductivity for WSM and SOC-NCM for different impurity types in the presence of parameter t_x . Plots are appropriately normalized.

The zero-LMC contour $\alpha_c(t_x)$ is qualitatively similar to the case of nonzero t_z , but nevertheless exhibits quantitative differences. In SOC-NCM, weak-sign-reversal is observed. Unlike the $t_z \neq 0$ case, we observe quantitative differences between non-magnetic and σ_z -impurities (Fig. 6 (b) and Fig. 6 (c)). Surprisingly, WSMs in the presence of σ_x or σ_y impurities, exhibit neither weak-sign-reversal nor strong-sign-reversal in the presence of t_x parameter (Fig. 6 (d)). This can be again understood from the fact that either of these impurity types changes the roles of internode scattering and that tilting the Weyl cone in a direction orthogonal to the direction of the magnetic field doesn't add an overall linear component to the magnetoconductivity. For SOC-NCM, we observe weak-sign-reversal, with quantitative differences between σ_x and σ_y impurities.

B. Planar Hall conductance

We next discuss the planar Hall conductance in SOC-NCM and compare the results with a standard WSM. In WSMs, the PHC can be expressed as [56]

$$\sigma_{xz}(B) = \sigma_{xz}^{(2)}(B - B_0)^2 + \sigma_{xz}^{(0)}, \quad (8)$$

where B_0 is the vertex of the parabola, and $\sigma_{xz}^{(2)}$ is the quadratic coefficient. The above form allows us to generalize PHC away from the origin, i.e., $B_0 \neq 0$. The

angular dependence for WSM is $\sin(2\gamma)$ for a point-like non-magnetic impurity profile. We find that this dependence is retained for magnetic impurities pointing in the z -direction as well (Fig. 7 (a)), and tilting the Weyl cones ($t_z \neq 0$) only has a quantitative effect. In contrast, SOC-NCMs have a qualitatively different dependence on t_z (Fig. 7 (b)). We observe that unlike in WSMs, the planar Hall conductance in SOC-NCMs exhibits weak-sign-reversal as a function of the parameter t_z . For σ_x and σ_y impurities, PHC in both WSMs and SOC-NCMs exhibit weak-sign-reversal and exhibit similar qualitative behavior (Fig. 7 (c) and (d)). In both systems, interband (internode) scattering is found to have no significant qualitative effect on planar Hall conductance.

For the nodes tilted along the x -direction, we observe qualitatively very different behavior. For σ_0 point-like impurities, the $\sin 2\gamma$ trend is observed irrespective of the value of t_x , as expected for Weyl cones that are oriented in the same direction. We find qualitatively similar behavior irrespective of the impurity type (Fig. 8 (a)). Note that if the Weyl cones were oriented opposite to each other, one instead finds a $\sin \gamma$ behavior of PHC [16]. In the case of SOC-NCMs, one finds a transition from $\sin 2\gamma$ trend to $\sin \gamma$ as the parameter t_x is increased from zero in either direction (Fig. 8). Like WSMs, we observe qualitatively similar behavior for both magnetic (any direction) and non-magnetic impurities.

C. Anomalous contribution to the Hall Conductance

In WSMs, the nonvanishing anomalous Hall conductance (AHC) has been attributed to the presence of a finite vector \mathbf{k}_0 that separates Weyl cones of opposite chiralities. The net AHC is given by $\sigma_{xy}^a = e^2 k_0 / h$. In the presence of time-reversal symmetry, multiple such vectors add up to zero, and AHC is zero. It is noteworthy that the intrinsic AHC contribution of one node, which is given by the integral of the Berry curvature of the filled band up to the Fermi surface, exactly cancels the contribution of the other node. The nonzero AHC in TR-broken WSMs is understood by considering a gapped 2D Chern insulator $H(\mathbf{k}_\perp, k_z)$ that undergoes a topological

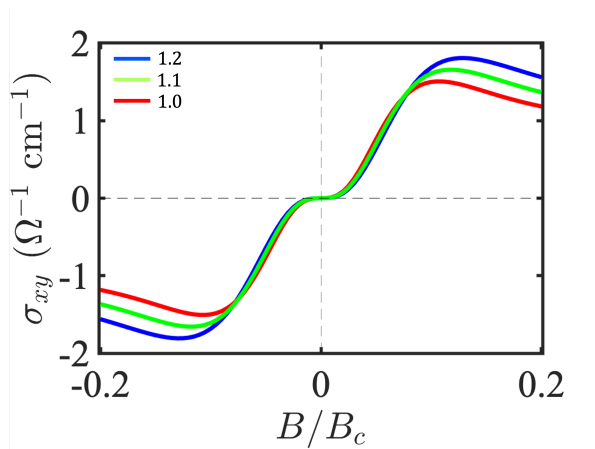


Figure 9. Geometrical contribution to the Hall conductivity showing a non-monotonic behavior. The legends indicate the strength of spin-orbit coupling parameter ϑ in units of 10^5ms^{-1} . We chose $g = 2$.

phase transition at the Weyl node [7].

In SOC-NCMs, we particularly focus on a single nodal point. It is expected that the two Fermi surfaces that enclose the nodal point cancel out their contributions of anomalous Hall conductivity, but as we show next, the presence of an external magnetic field induces finite anomalous contribution to the Hall conductivity. In the presence of an external magnetic field, Zeeman coupling will introduce an additional term in the Hamiltonian given by [58–60]

$$H_z = -g\mu_B \boldsymbol{\sigma} \cdot \mathbf{B}. \quad (9)$$

This causes an opposite energy shift in both bands. Furthermore, the anomalous shift in the energy dispersion due to the orbital magnetic moment ($\epsilon_{\mathbf{k}}^\lambda \rightarrow \epsilon_{\mathbf{k}}^\lambda - \mathbf{m}_{\mathbf{k}}^\lambda \cdot \mathbf{B}$). Both of these effects, in concurrence, lead to a finite and measurable anomalous contribution to the Hall conductance, which at zero temperature is calculated as

$$\sigma_{xy}^a = \frac{e^2}{\hbar} \sum_{\lambda=\pm 1} \int \frac{d^3\mathbf{k}}{(2\pi)^3} \mathcal{D}_{\mathbf{k}}^\lambda \theta(\epsilon_F - \epsilon_{\mathbf{k}}^\lambda) \Omega_z^\lambda(\mathbf{k}), \quad (10)$$

where $\mathcal{D}_{\mathbf{k}}^\lambda = (1 + e\mathbf{B} \cdot \boldsymbol{\Omega}_{\mathbf{k}}^\lambda / \hbar)$. In Fig. 9 we plot the geometrical contribution to the Hall conductivity for SOC-NCM as evaluated from Eq. 10. Interestingly, the behavior is non-monotonic with respect to the magnetic field, and for low enough magnetic field, the anomalous contribution is found to be independent of the strength of the spin-orbit coupling parameter. The non-monotonicity can be understood as follows. With increasing magnitude of the magnetic field, the net Berry curvature contribution increases, but eventually decreases as for larger magnetic fields as the magnitude of the Berry curvature itself reduces. This can be easily tested in current and upcoming transport experiments in SOC-NCMs.

IV. CONCLUSIONS AND DISCUSSIONS

Chiral anomaly is a Fermi surface property with similar characteristics in Weyl and spin-orbit coupled non-centrosymmetric metals. It manifests itself in the measurement of longitudinal magnetoconductance and the planar Hall conductance. However, in striking contrast to WSMs, where the sign of the LMC is sensitive to the internode scattering strength, the sign of the LMC in SOC-NCMs is independent of the interband scattering strength and always remains positive. The reason is traced down to the subtle difference in the orbital magnetic moment in WSMs and SOC-NCMs. Orbital magnetic moment in SOC-NCMs is of equal magnitudes and signs in both the bands but has opposite signs at the two nodes in WSMs. This difference also yields drastic differences in other transport properties, such as the planar Hall conductivity. We also examined all the properties in the presence of a tilt parameter (t_z and t_x) and for different impurity types (magnetic and non-magnetic). The behavior for σ_0 and σ_z impurities was found to be qualitatively similar to each other as they do not flip with chirality. On the other hand, σ_x and σ_y flip the chirality and behave qualitatively similar to each other. Lastly, we predict that the combination of the anomalous orbital magnetic moment and the Zeeman field gives rise to a geometrical contribution to the Hall conductivity in SOC-NCMs that is non-monotonic in the magnetic field. Our study is highly pertinent in light of current and upcoming experiments in the field of spin-orbit coupled noncentrosymmetric and Weyl metals.

Acknowledgements G.V.K. and A.A. acknowledge financial support from IIT Mandi HTRA. G.S. acknowledges support from IIT Mandi Seed Grant. We thank Shubhanshu Karoliya for his technical support.

Appendix A: Maxwell Boltzmann transport theory

Due to Berry phase effects, in the presence of electric and magnetic fields, the semiclassical dynamics of the Bloch electrons are modified and governed by the following equation [19, 28].

$$\begin{aligned} \dot{\mathbf{r}}^\lambda &= \mathcal{D}^\lambda \left(\frac{e}{\hbar} (\mathbf{E} \times \boldsymbol{\Omega}^\lambda) + \frac{e}{\hbar} (\mathbf{v}^\lambda \cdot \boldsymbol{\Omega}^\lambda) \mathbf{B} + \mathbf{v}_{\mathbf{k}}^\lambda \right) \\ \dot{\mathbf{p}}^\lambda &= -e\mathcal{D}^\lambda \left(\mathbf{E} + \mathbf{v}_{\mathbf{k}}^\lambda \times \mathbf{B} + \frac{e}{\hbar} (\mathbf{E} \cdot \mathbf{B}) \boldsymbol{\Omega}^\lambda \right). \end{aligned} \quad (\text{A1})$$

where $\mathbf{v}_{\mathbf{k}}^\lambda = \frac{1}{\hbar} \frac{\partial \epsilon_{\mathbf{k}}^\lambda(\mathbf{k})}{\partial \mathbf{k}}$ is the band velocity, $\boldsymbol{\Omega}^\lambda = -\lambda \mathbf{k} / 2k^3$ is the Berry curvature, and $\mathcal{D}^\lambda = (1 + e\mathbf{B} \cdot \boldsymbol{\Omega}^\lambda / \hbar)^{-1}$ is the factor modifying the density of the states in the presence of the Berry curvature. The self-rotation of the Bloch wave packet also gives rise to an orbital magnetic moment, $\mathbf{m}_{\mathbf{k}}^\lambda$ [61]. In the presence of a magnetic field, the orbital magnetic moment shifts the energy dispersion as $\epsilon_{\mathbf{k}}^\lambda \rightarrow \epsilon_{\mathbf{k}}^\lambda - \mathbf{m}_{\mathbf{k}}^\lambda \cdot \mathbf{B}$. Using Eq. A1 and Eq. 6 and retaining terms only up to linear order in electric and magnetic

fields, the Boltzmann transport equation becomes

$$\begin{aligned} & \left[\left(\frac{\partial f_0^\lambda}{\partial \epsilon_{\mathbf{k}}^\lambda} \right) \mathbf{E} \cdot \left(\mathbf{v}_{\mathbf{k}}^\lambda + \frac{e\mathbf{B}}{\hbar} (\boldsymbol{\Omega}^\lambda \cdot \mathbf{v}_{\mathbf{k}}^\lambda) \right) \right] \\ & = -\frac{1}{e\mathcal{D}^\lambda} \sum_{\lambda'} \sum_{\mathbf{k}'} W_{\mathbf{k}\mathbf{k}'}^{\lambda\lambda'} (g_{\mathbf{k}'}^\lambda - g_{\mathbf{k}}^\lambda) \end{aligned} \quad (\text{A2})$$

We have fixed the direction of the electric field along increasing x -direction, and the magnetic field is rotated in xz -plane (See Fig. 3). Therefore, $\mathbf{E} = E(0, 0, 1)$ and $\mathbf{B} = B(\cos \gamma, 0, \sin \gamma)$. In this case, only the z -component of $\boldsymbol{\Lambda}$ is relevant. Therefore Eq. A2 reduces to,

$$\mathcal{D}^\lambda(k) \left[v_{\mathbf{k}}^{\lambda,z} + \frac{eB \sin \gamma}{\hbar} (\mathbf{v}_{\mathbf{k}}^\lambda \cdot \boldsymbol{\Omega}_k^\lambda) \right] = \sum_{\lambda' \mathbf{k}'} \mathbf{W}_{\mathbf{k}\mathbf{k}'}^{\lambda\lambda'} (\Lambda_{\mathbf{k}'}^{\lambda'} - \Lambda_{\mathbf{k}}^\lambda). \quad (\text{A3})$$

We define the valley scattering time ($\tau_{\mathbf{k}}^\lambda$) as follows

$$\frac{1}{\tau_{\mathbf{k}}^\lambda(\theta, \phi)} = \sum_{\lambda'} \mathcal{V} \int \frac{d^3 \mathbf{k}'}{(2\pi)^3} (\mathcal{D}_{\mathbf{k}'}^{\lambda'})^{-1} \mathbf{W}_{\mathbf{k}\mathbf{k}'}^{\lambda\lambda'} \quad (\text{A4})$$

$\mathbf{W}_{\mathbf{k}\mathbf{k}'}^{\lambda\lambda'}$ is defined in Eq. 7 and the corresponding overlap of the Bloch wave-function is $\mathcal{G}_i^{\lambda\lambda'}(\theta, \phi) = [1 + \lambda\lambda' \xi_i (\cos \theta \cos \theta' + \alpha_i \sin \theta \sin \theta' \cos \phi \cos \phi' + \beta_i \sin \theta \sin \theta' \sin \phi \sin \phi')] \text{ with } i = 0, 1, 2, 3$ (Please see Tab. I). Taking Berry phase into account and corresponding change in the density of states, $\sum_{\mathbf{k}} \rightarrow \mathcal{V} \int \frac{d^3 \mathbf{k}}{(2\pi)^3} \mathcal{D}^\lambda(k)$, Eq. A3 becomes

$$\begin{aligned} & h_\mu^\lambda(\theta, \phi) + \frac{\Lambda_{\mu,i}^\lambda(\theta, \phi)}{\tau_{\mu,i}^\lambda(\theta, \phi)} \\ & = \sum_{\lambda'} \mathcal{V} \int \frac{d^3 \mathbf{k}'}{(2\pi)^3} \mathcal{D}^{\lambda'}(k') \mathbf{W}_{\mathbf{k}\mathbf{k}'}^{\lambda\lambda'} \Lambda_{\mu,i}^{\lambda'}(\theta', \phi') \end{aligned} \quad (\text{A5})$$

Here $h_\mu^\lambda(\theta, \phi) = \mathcal{D}^{\lambda\kappa} [v_{z,\mathbf{k}}^\lambda + eB \sin \gamma (\boldsymbol{\Omega}_k^\lambda \cdot \mathbf{v}_{\mathbf{k}}^\lambda)]$. In the zero-temperature limit, for a constant Fermi energy surface, Eq. A4 and RHS of Eq. A5 is reduced to the integration

over θ' and ϕ' :

$$\frac{1}{\tau_{\mu,i}^\lambda(\theta, \phi)} = \mathcal{V} \sum_{\lambda'} \Pi^{\lambda\lambda'} \iint \frac{(k')^3 \sin \theta'}{|\mathbf{v}_{\mathbf{k}'}^{\lambda'} \cdot \mathbf{k}'^{\lambda'}|} d\theta' d\phi' \mathcal{G}_i^{\lambda\lambda'} (D_{\mathbf{k}'}^{\lambda'})^{-1} \quad (\text{A6})$$

$$\begin{aligned} & \mathcal{V} \sum_{\lambda'} \Pi^{\lambda\lambda'} \iint f^{\lambda'}(\theta', \phi') \mathcal{G}_i^{\lambda\lambda'} d\theta' d\phi' \times [d^{\lambda'} - h_\mu^{\lambda'}(\theta', \phi') \\ & + a^{\lambda'} \cos \theta' + b^{\lambda'} \sin \theta' \cos \phi' + c^{\lambda'} \sin \theta' \sin \phi'] \end{aligned} \quad (\text{A7})$$

where $\Pi^{\lambda\lambda'} = N|U^{\lambda\lambda'}|^2/4\pi^2\hbar^2$, $f^\lambda(\theta, \phi) = \frac{(k)^3}{|\mathbf{v}_{\mathbf{k}}^\lambda \cdot \mathbf{k}^\lambda|} \sin \theta (\mathcal{D}_{\mathbf{k}}^\lambda)^{-1} \tau_\mu^\lambda(\theta, \phi)$. Using ansatz $\Lambda_{\mathbf{k}}^\lambda = [d^\lambda - h_{\mathbf{k}}^\lambda + a^\lambda \cos \phi + b^\lambda \sin \theta \cos \phi + c^\lambda \sin \theta \sin \phi] \tau_\mu^\lambda(\theta, \phi)$ the above equation is written in the following form:

$$\begin{aligned} & d^\lambda + a^\lambda \cos \phi + b^\lambda \sin \theta \cos \phi + c^\lambda \sin \theta \sin \phi \\ & = \sum_{\lambda'} \mathcal{V} \Pi^{\lambda\lambda'} \iint f^{\lambda'}(\theta', \phi') d\theta' d\phi' \\ & \times [d^{\lambda'} - h_{\mathbf{k}'}^{\lambda'} + a^{\lambda'} \cos \theta' + b^{\lambda'} \sin \theta' \cos \phi' + c^{\lambda'} \sin \theta' \sin \phi'] \end{aligned} \quad (\text{A8})$$

When the aforementioned equation is explicitly put out (for each value of i), it appears as seven simultaneous equations that must be solved for eight variables. The particle number conservation provides another restriction:

$$\sum_{\lambda} \sum_{\mathbf{k}} g_{\mathbf{k}}^\lambda = 0 \quad (\text{A9})$$

For the eight unknowns ($d^{\pm 1}, a^{\pm 1}, b^{\pm 1}, c^{\pm 1}$), equations A8 and A9 are simultaneously solved with Eq. A6. Due to the intricate structure of the equations, all two-dimensional integrals with respect to θ' and ϕ' the simultaneous equations' solution are carried out numerically.

i	σ_i	α_i	β_i	ξ_i
0	$\mathbb{I}_{2 \times 2}$	+1	+1	+1
1	σ_x	-1	+1	-1
2	σ_y	+1	-1	-1
3	σ_z	-1	-1	+1

Table I. The signs of α, β , and ξ are used in the expression of overlap of the Bloch wave function (see Eq. A4). $\sigma_{x,y,z}$ are the components of the Pauli spin vector, and $\mathbb{I}_{2 \times 2}$ is the identity matrix.

- [1] S. L. Adler, Axial-vector vertex in spinor electrodynamics, *Physical Review* **177**, 2426 (1969).
- [2] J. S. Bell and R. Jackiw, A pcac puzzle: $\pi \rightarrow \gamma\gamma$ in the σ -model, *Il Nuovo Cimento A (1965-1970)* **60**, 47 (1969).
- [3] N. Armitage, E. Mele, and A. Vishwanath, Weyl and dirac semimetals in three-dimensional solids, *Reviews of Modern Physics* **90**, 015001 (2018).
- [4] G. E. Volovik, *The universe in a helium droplet*, Vol. 117 (Oxford University Press on Demand, 2003).
- [5] H. B. Nielsen and M. Ninomiya, *No-go theorem for regularizing chiral fermions*, Tech. Rep. (Science Research Council, 1981).
- [6] H. B. Nielsen and M. Ninomiya, The adler-bell-jackiw anomaly and weyl fermions in a crystal, *Physics Letters B* **130**, 389 (1983).
- [7] X. Wan, A. M. Turner, A. Vishwanath, and S. Y. Savrasov, Topological semimetal and fermi-arc surface states in the electronic structure of pyrochlore iridates, *Physical Review B* **83**, 205101 (2011).
- [8] G. Xu, H. Weng, Z. Wang, X. Dai, and Z. Fang, Chern semimetal and the quantized anomalous hall effect in hgr 2 se 4, *Physical Review Letters* **107**, 186806 (2011).
- [9] A. Zyuzin, S. Wu, and A. Burkov, Weyl semimetal with broken time reversal and inversion symmetries, *Physical Review B* **85**, 165110 (2012).
- [10] D. Son and B. Spivak, Chiral anomaly and classical negative magnetoresistance of weyl metals, *Physical Review B* **88**, 104412 (2013).
- [11] K.-S. Kim, H.-J. Kim, and M. Sasaki, Boltzmann equation approach to anomalous transport in a weyl metal, *Physical Review B* **89**, 195137 (2014).
- [12] R. Lundgren, P. Laurell, and G. A. Fiete, Thermoelectric properties of weyl and dirac semimetals, *Physical Review B* **90**, 165115 (2014).
- [13] A. Cortijo, Linear magnetochiral effect in weyl semimetals, *Physical Review B* **94**, 241105 (2016).
- [14] G. Sharma, P. Goswami, and S. Tewari, Nernst and magnetothermal conductivity in a lattice model of weyl fermions, *Physical Review B* **93**, 035116 (2016).
- [15] V. A. Zyuzin, Magnetotransport of weyl semimetals due to the chiral anomaly, *Physical Review B* **95**, 245128 (2017).
- [16] S. Nandy, G. Sharma, A. Taraphder, and S. Tewari, Chiral anomaly as the origin of the planar hall effect in weyl semimetals, *Physical Review Letters* **119**, 176804 (2017).
- [17] K. Das and A. Agarwal, Berry curvature induced thermopower in type-i and type-ii weyl semimetals, *Physical Review B* **100**, 085406 (2019).
- [18] A. Kundu, Z. B. Siu, H. Yang, and M. B. Jalil, Magnetotransport of weyl semimetals with tilted dirac cones, *New Journal of Physics* **22**, 083081 (2020).
- [19] A. Knoll, C. Timm, and T. Meng, Negative longitudinal magnetoconductance at weak fields in weyl semimetals, *Physical Review B* **101**, 201402 (2020).
- [20] G. Sharma, S. Nandy, and S. Tewari, Sign of longitudinal magnetoconductivity and the planar hall effect in weyl semimetals, *Physical Review B* **102**, 205107 (2020).
- [21] G. Bednik, K. Tikhonov, and S. Syzranov, Magnetotransport and internodal tunnelling in weyl semimetals, *Physical Review Research* **2**, 023124 (2020).
- [22] L. He, X. Hong, J. Dong, J. Pan, Z. Zhang, J. Zhang, and S. Li, Quantum transport evidence for the three-dimensional dirac semimetal phase in cd 3 as 2, *Physical Review Letters* **113**, 246402 (2014).
- [23] T. Liang, Q. Gibson, M. N. Ali, M. Liu, R. J. Cava, and N. P. Ong, Ultrahigh mobility and giant magnetoresistance in the dirac semimetal cd 3 as 2, *Nature materials* **14**, 280 (2015).
- [24] C.-L. Zhang, S.-Y. Xu, I. Belopolski, Z. Yuan, Z. Lin, B. Tong, G. Bian, N. Alidoust, C.-C. Lee, S.-M. Huang, *et al.*, Signatures of the adler–bell–jackiw chiral anomaly in a weyl fermion semimetal, *Nature communications* **7**, 1 (2016).
- [25] Q. Li, D. E. Kharzeev, C. Zhang, Y. Huang, I. Pletikosić, A. Fedorov, R. Zhong, J. Schneeloch, G. Gu, and T. Valla, Chiral magnetic effect in zрте 5, *Nature Physics* **12**, 550 (2016).
- [26] J. Xiong, S. K. Kushwaha, T. Liang, J. W. Krizan, M. Hirschberger, W. Wang, R. J. Cava, and N. P. Ong, Evidence for the chiral anomaly in the dirac semimetal na3bi, *Science* **350**, 413 (2015).
- [27] M. Hirschberger, S. Kushwaha, Z. Wang, Q. Gibson, S. Liang, C. A. Belvin, B. A. Bernevig, R. J. Cava, and N. P. Ong, The chiral anomaly and thermopower of weyl fermions in the half-heusler gdptbi, *Nature materials* **15**, 1161 (2016).
- [28] D. T. Son and N. Yamamoto, Berry curvature, triangle anomalies, and the chiral magnetic effect in fermi liquids, *Physical Review Letters* **109**, 181602 (2012).
- [29] P. Goswami and S. Tewari, Axionic field theory of (3+1)-dimensional weyl semimetals, *Physical Review B* **88**, 245107 (2013).
- [30] P. Goswami, J. Pixley, and S. D. Sarma, Axial anomaly and longitudinal magnetoresistance of a generic three-dimensional metal, *Physical Review B* **92**, 075205 (2015).
- [31] S. Zhong, J. Orenstein, and J. E. Moore, Optical gyrotropy from axion electrodynamics in momentum space, *Physical Review Letters* **115**, 117403 (2015).
- [32] P. Goswami, G. Sharma, and S. Tewari, Optical activity as a test for dynamic chiral magnetic effect of weyl semimetals, *Physical Review B* **92**, 161110 (2015).
- [33] A. L. Levy, A. B. Sushkov, F. Liu, B. Shen, N. Ni, H. D. Drew, and G. S. Jenkins, Optical evidence of the chiral magnetic anomaly in the weyl semimetal taas, *Physical Review B* **101**, 125102 (2020).
- [34] J.-M. Parent, R. Côté, and I. Garate, Magneto-optical kerr effect and signature of the chiral anomaly in a weyl semimetal in magnetic field, *Physical Review B* **102**, 245126 (2020).
- [35] Z. Song, J. Zhao, Z. Fang, and X. Dai, Detecting the chiral magnetic effect by lattice dynamics in weyl semimetals, *Physical Review B* **94**, 214306 (2016).
- [36] P. Rinkel, P. L. Lopes, and I. Garate, Signatures of the chiral anomaly in phonon dynamics, *Physical Review Letters* **119**, 107401 (2017).
- [37] X. Yuan, C. Zhang, Y. Zhang, Z. Yan, T. Lyu, M. Zhang, Z. Li, C. Song, M. Zhao, P. Leng, *et al.*, The discovery of dynamic chiral anomaly in a weyl semimetal nbas, *Nature communications* **11**, 1 (2020).
- [38] B. Cheng, T. Schumann, S. Stemmer, and N. Armitage, Probing charge pumping and relaxation of the chiral anomaly in a dirac semimetal, arXiv preprint

- arXiv:1910.13655 (2019).
- [39] K. Fujikawa and H. Suzuki, *Path integrals and quantum anomalies*, 122 (Oxford University Press, 2004).
- [40] Y. Gao, S. A. Yang, and Q. Niu, Intrinsic relative magnetoconductivity of nonmagnetic metals, *Physical Review B* **95**, 165135 (2017).
- [41] X. Dai, Z. Du, and H.-Z. Lu, Negative magnetoresistance without chiral anomaly in topological insulators, *Physical review letters* **119**, 166601 (2017).
- [42] A. Andreev and B. Spivak, Longitudinal negative magnetoresistance and magnetotransport phenomena in conventional and topological conductors, *Physical review letters* **120**, 026601 (2018).
- [43] H.-W. Wang, B. Fu, and S.-Q. Shen, Intrinsic magnetoresistance in three-dimensional dirac materials with low carrier density, *Physical Review B* **98**, 081202 (2018).
- [44] S. Nandy, A. Taraphder, and S. Tewari, Berry phase theory of planar hall effect in topological insulators, *Scientific Reports* **8**, 14983 (2018).
- [45] B. Fu, H.-W. Wang, and S.-Q. Shen, Quantum magnetotransport in massive dirac materials, *Physical Review B* **101**, 125203 (2020).
- [46] O. Pal, B. Dey, and T. K. Ghosh, Berry curvature induced magnetotransport in 3d noncentrosymmetric metals, *Journal of Physics: Condensed Matter* **34**, 025702 (2021).
- [47] H.-W. Wang, B. Fu, and S.-Q. Shen, Helical symmetry breaking and quantum anomaly in massive dirac fermions, *Physical Review B* **104**, L241111 (2021).
- [48] S. Cheon, G. Y. Cho, K.-S. Kim, and H.-W. Lee, Chiral anomaly in noncentrosymmetric systems induced by spin-orbit coupling, *Phys. Rev. B* **105**, L180303 (2022).
- [49] S. Das, K. Das, and A. Agarwal, Chiral anomalies in three-dimensional spin-orbit coupled metals: Electrical, thermal, and gravitational anomalies, *Physical Review B* **108**, 045405 (2023).
- [50] H.-Z. Lu, S.-B. Zhang, and S.-Q. Shen, High-field magnetoconductivity of topological semimetals with short-range potential, *Physical Review B* **92**, 045203 (2015).
- [51] C.-Z. Chen, H. Liu, H. Jiang, and X. Xie, Positive magnetoconductivity of weyl semimetals in the ultraquantum limit, *Physical Review B* **93**, 165420 (2016).
- [52] S.-B. Zhang, H.-Z. Lu, and S.-Q. Shen, Linear magnetoconductivity in an intrinsic topological weyl semimetal, *New Journal of Physics* **18**, 053039 (2016).
- [53] J. Shao and L. Yan, Magneto-conductivity of tilted type-i weyl semimetals with different types of impurities, *AIP Advances* **9**, 045319 (2019).
- [54] X. Li, B. Roy, and S. D. Sarma, Weyl fermions with arbitrary monopoles in magnetic fields: Landau levels, longitudinal magnetotransport, and density-wave ordering, *Physical Review B* **94**, 195144 (2016).
- [55] X.-T. Ji, H.-Z. Lu, Z.-G. Zhu, and G. Su, Effect of the screened coulomb disorder on magneto-transport in weyl semimetals, *Journal of Applied Physics* **123**, 203901 (2018).
- [56] A. Ahmad, K. V. Raman, S. Tewari, and G. Sharma, Longitudinal magnetoconductance and the planar hall conductance in inhomogeneous weyl semimetals, *Physical Review B* **107**, 144206 (2023).
- [57] C. Xiao, H. Chen, Y. Gao, D. Xiao, A. H. MacDonald, and Q. Niu, Linear magnetoresistance induced by intrascattering semiclassics of bloch electrons, *Physical Review B* **101**, 201410 (2020).
- [58] G. Sharma, C. Moore, S. Saha, and S. Tewari, Nernst effect in dirac and inversion-asymmetric weyl semimetals, *Physical Review B* **96**, 195119 (2017).
- [59] G. Sharma, Tunable topological nernst effect in two-dimensional transition-metal dichalcogenides, *Physical Review B* **98**, 075416 (2018).
- [60] K. Gadge, S. Tewari, and G. Sharma, Anomalous hall and nernst effects in kane fermions, *Physical Review B* **105**, 235420 (2022).
- [61] D. Xiao, M.-C. Chang, and Q. Niu, Berry phase effects on electronic properties, *Reviews of modern physics* **82**, 1959 (2010).